Sinuous distortion of vortex surfaces in the lateral growth of turbulent spots

Yaomin Zhao,[1] Shiying Xiong,[1] Yue Yang,[1,2,*] and Shiyi Chen[1,2,3]

[1]*State Key Laboratory for Turbulence and Complex Systems, College of Engineering, Peking University, Beijing 100871, China*

[2]*CAPT and BIC-EAST, Peking University, Beijing 100871, China*

[3]*Department of Mechanics and Aerospace Engineering, South University of Science and Technology of China, Shenzhen 518055, China*

(Received 9 January 2018; published 11 July 2018)

We extend the vortex-surface field (VSF), a Lagrangian-based structure-identification method, to study the structural evolution in Klebanoff-type boundary-layer transition. The VSF is constructed from the instantaneous vorticity fields in a series of sliding windows at different times and streamwise locations using the boundary-constraint method. The visualization of VSF isosurfaces displays the Lagrangian-like evolution of vortex surfaces consisting of vortex lines. The near-wall VSF isosurfaces evolve from wall-parallel planar vortex surfaces through a train of hairpin-like structures into turbulent spots. In the inception of turbulent spots, the train of hairpin-like bulges of vortex surfaces induces sinuous spanwise perturbations on the adjacent flank of lower wavy vortex surfaces, and then triggers the Kelvin-Helmholtz instability in the spanwise direction. The resultant sinuous distortion of vortex surfaces propagates in the spanwise direction, which can lead to the mass production of small-scale, skewed hairpin-like structures and the rapid lateral growth of turbulent spots. The streaky and hairpin-like structures have strong interactions in the present Klebanoff-type transition. On the other hand, these signature structures can be interpreted as different evolutionary geometries of the same set of VSF isosurfaces at different times and spatial regions, rather than considering them as two different elementary structures visualized by different structure-identification methods. Furthermore, the quantified distortion of near-wall vortex surfaces in the lateral growth of young turbulent spots is highly correlated to the surge of the skin-friction coefficient in the transition.

DOI: 10.1103/PhysRevFluids.3.074701

I. INTRODUCTION

The generation of turbulent spots is a critical process in boundary-layer transition. This process is often described as an abrupt structural transition from relatively isolated and ordered flow structures, such as quasistreamwise vortices, hairpin vortices, and streaks of high- and low-speed velocity, to chaotic, multiscale structures in a finite region spanning several boundary-layer thicknesses. The inception of turbulent spots is also important in flow dynamics and various engineering applications, because it signals the rapid increase of the skin friction in transition.

Although the boundary-layer transition has been extensively studied, there is no consensus on the accepted geometry of crucial coherent structures and the generation mechanism of turbulent spots. In general, three mechanisms for the generation of turbulent spots have been reported in the literature, as follows.

*yyg@pku.edu.cn

(1) The hairpin-like structure has been accepted as an important structure in turbulent boundary layers [1], and the self-induction of hairpin-like structures can form complex structure packets [2,3]. Singer and Joslin [4] observed that the growth of a hairpin vortex generates offspring vortices near their "legs," and they eventually form a prematured turbulent spot. Subsequently new hairpin-like structures at smaller scales are regenerated at the lateral edge of the growing turbulent spot [5,6].

(2) The streaky structure elongated in the streamwise direction has also been considered to play a key role in the sustainment of turbulence in wall-bounded flows [7,8], and the instability of these streaky structures can be critical in different transition scenarios [9–11]. Zaki *et al.* [12,13] argued that free-stream vortical disturbances in bypass transition trigger the instability of streamwise streaks, and then the instability causes the formation of turbulent spots. Schoppa and Hussain [14] analyzed the dynamics for the transient growth of streaky instability, and Wang *et al.* [15] found that streamwise streaks with spanwise perturbations can evolve into hairpin-like structures under the streak-transient-growth mechanism.

(3) Recently several studies realized that both hairpin-like and streaky structures are important in wall flows, and their interactions can be a dominant mechanism for the generation of turbulent spots. Schröder *et al.* [16,17] observed that both hairpins and streaks are prominent in a flat-plate turbulent boundary layer and proposed a hairpin-regeneration model indicating that the interaction between the two types of structures is responsible for the self-sustained process of the wall-normal flow transportation. Brinkerhoff and Yaras [18] concluded that the lateral growth of turbulent spots is primarily due to the coupling of the regeneration of hairpin-like structures and the spanwise shear-layer instability. Wu *et al.* [19] pointed out that the infant turbulent spot is first initiated by the Λ-like structure arising from spanwise vortex filaments, and the meandering and breakdown of streaky structures are triggered by vortical structures inside turbulent spots.

The different interpretations of the generation mechanism of turbulent spots are partly due to the flow structures visualized by different identification methods. In general, streaky structures are identified by the streamwise velocity, wall-normal velocity, temperature, or other passive scalars, while vortical structures are identified by vortex identification criteria based on the Eulerian velocity gradient tensor such as the Q, λ_2, and λ_{ci} criteria [3,20,21]. The various structure identification methods have their own strengths and weaknesses. For example, the passive scalars have the Lagrangian-like nature, such as dye and hydrogen bubbles used in experimental visualization [22], but they face difficulties of significant scalar diffusion in high-shear regions and lack exact connections between scalar patterns and vortical structures. The Eulerian vortex identification criteria can effectively identify intense local rotational regions or "vortex cores" and can be easily implemented, but the identified structures at a fixed isocontour level at different times may lack time coherence to elucidate the continuous dynamics of coherent structures. Moreover, a bundle of vortex lines can reveal vorticity dynamics in the early transitional stage [14,23,24], but in the late transitional or fully turbulent stage, it is difficult to objectively select seed points so that the chaotic vortex lines have a uniform spatial density to display smooth coherent structures.

The very different structure identification methods introduce ambiguity and incompleteness in the structure characterization of turbulent spots perhaps composed of both streaks and vortices with strong interactions with each other. Although a carefully selected combination of different structure-identification methods [11,14,19,25,26] can partly alleviate the issues in the structure characterization, the selection of identification methods and isocontour levels is still subjective [27]. Consequently, different interpretations of structural evolution can result in the continued debate about the generation mechanism of turbulent spots, and a clear dynamical description of the interaction between near-wall vortical structures and streaks remains elusive [19].

In order to tackle the issues of the structure characterization, the vortex-surface field (VSF) is developed for studying the Lagrangian-like evolution of vortical structures [28,29]. Every isosurface of the VSF is defined as a vortex surface consisting of vortex lines. A typical VSF visualization uses evolving vortex surfaces along with attached vortex lines and their vorticity magnitude to characterize vortical structures, which combines the strengths of different identification methods used in wall turbulence and has a special feature for displaying the Lagrangian-like temporal evolution of a

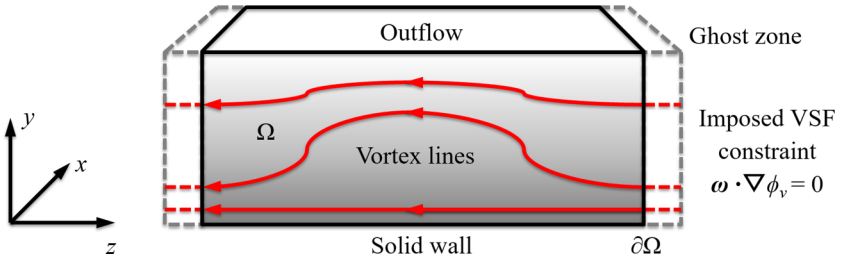

FIG. 1. Schematic diagram of the boundary-constraint method for constructing the VSF in a boundary layer.

uniquely defined VSF isosurface with a fixed isocontour value. The VSF has been applied to the Klebanoff-type (K-type) transition in channel flow to elucidate the continuous temporal evolution of vortical structures from a Lagrangian perspective [24,30].

In the present study, we extend the VSF to investigate the Lagrangian-like structural evolution in the K-type transitional boundary layer [31], as a first VSF study on the canonical boundary layer. Specifically, the boundary-constraint method and the sliding window are developed to efficiently construct VSFs from a large-scale database of the direct numerical simulation (DNS). We will elucidate the generation mechanism of turbulent spots using the evolutionary geometry of initially wall-parallel vortex surfaces, instead of using the "streaks" and "hairpins" with presumed geometries identified by different methods. Furthermore, we explore the quantitative relationship between the deformation of vortex surfaces and the rise of the skin-friction coefficient in the generation of turbulent spots.

The outline of this paper is as follows. In Sec. II we describe numerical methods for constructing VSFs using the boundary-constraint method and extracting vorticity fields from the full DNS database using the sliding window. In Sec. III we visualize the VSF isosurfaces and explain the growth mechanism of turbulent spots. Some conclusions are drawn in Sec. IV.

II. NUMERICAL OVERVIEW

A. The boundary-constraint method

Given an instantaneous three-dimensional vorticity field $\boldsymbol{\omega}(\boldsymbol{x},t)$ at a time instant t, the VSF ϕ_v is defined to satisfy the constraint [28]

$$\mathcal{C}_v \equiv \boldsymbol{\omega}\cdot\nabla\phi_v = 0, \tag{1}$$

i.e., the vorticity vector is perpendicular to the normal direction of the VSF isosurface everywhere. In other words, $\boldsymbol{\omega}$ is tangent to the isosurface of ϕ_v, and every isosurface of ϕ_v is a vortex surface consisting of vortex lines. We remark that the exact VSF solution must exist for a given instantaneous flow field with vanishing helicity density $\boldsymbol{u}\cdot\boldsymbol{\omega} = 0$ but the solution is not unique [28], so additional constraints should be considered to determine a unique ϕ_v in a specific flow [24]. For a general velocity field with $\boldsymbol{u}\cdot\boldsymbol{\omega} \neq 0$, we have to seek an approximate VSF solution using numerical methods, which can be challenging and computationally expansive.

The boundary-constraint method [32] is developed to construct a VSF from instantaneous $\boldsymbol{\omega}(\boldsymbol{x},t)$ in shear flows. If appropriate boundary conditions of velocity and vorticity are satisfied, the VSFs constructed from separate vorticity fields at different times can still represent a Lagrangian-like temporal evolution of the VSF governed by a scalar transport equation. The boundary-constraint method can significantly reduce the demanding computational cost and required velocity data size, compared with the two-time method for solving evolution equations of the VSF [29] from a series of temporally resolved velocity fields.

The schematic diagram of the boundary-constraint method for constructing the VSF in a boundary layer is sketched in Fig. 1, where x, y, and z denote streamwise, wall-normal, and spanwise

coordinates, respectively. The VSF constraint $\mathcal{C}_v = 0$ is imposed at the lateral boundary $\partial\Omega$ and then transported into the computational domain Ω in pseudotime τ using the frozen vorticity field as

$$\frac{\partial \phi_v(\boldsymbol{x},t;\tau)}{\partial \tau} + \boldsymbol{\omega}(\boldsymbol{x},t)\cdot\nabla\phi_v(\boldsymbol{x},t;\tau) = 0,\ \ \boldsymbol{x}\in\Omega,\tau>0, \tag{2}$$

$$\boldsymbol{\omega}(\boldsymbol{x},t)\cdot\nabla\phi_v(\boldsymbol{x},t;\tau) = 0,\ \ \boldsymbol{x}\in\partial\Omega,\tau>0, \tag{3}$$

$$\phi_v(\boldsymbol{x},t;\tau) = \phi_{v0}(\boldsymbol{x},t),\ \ \boldsymbol{x}\in\Omega,\tau=0, \tag{4}$$

where $\phi_{v0}(\boldsymbol{x},t)$ is a given initial condition at $\tau = 0$. The corresponding transport equation for $\mathcal{C}_v$ has the same form as Eq. (2) with $\mathcal{C}_v = 0$ at boundaries. Thus, $\phi_v(\boldsymbol{x},t;\tau)$ can converge to a VSF solution at a large pseudotime through the pseudotransport as $\phi_v(\boldsymbol{x},t) = \lim_{\tau\to T_\tau}\phi_v(\boldsymbol{x},t;\tau)$ if all the vortex lines started from the boundary $\partial\Omega$ are ergodic within Ω. The maximum pseudotime T_τ depends on the given error tolerance of the VSF solution.

In the numerical implementation, Eq. (2) is advanced in τ using the third-order total-variation-diminishing Runge-Kutta method, and the convection term is treated by the fifth-order weighted essentially nonoscillatory (WENO) scheme [33]. The numerical diffusion in the WENO scheme can serve as a numerical dissipative regularization for Eq. (2). Moreover, in order to increase the computational accuracy and efficiency in the calculation of Eq. (2), two ghost zones are added next to the lateral boundaries of the computation domain, in which vortex lines are stretched to be normal to lateral boundaries of the ghost zones. More details of the boundary-constraint method can be found in Ref. [32].

B. Extraction of vorticity fields using the sliding window

The calculation of VSFs is implemented as a postprocessing step based on a time series of instantaneous velocity-vorticity fields in DNS [29,30]. In the present study, the boundary-constraint method is applied to construct VSFs from the DNS database of the K-type transition in a zero-pressure-gradient and spatially developed flat-plate boundary layer [31].

In the DNS, the nondimensionalized fully compressible Navier-Stokes equations are solved with the fourth-order finite difference scheme. The velocity $\boldsymbol{u} = (u,v,w)$ is nondimensionalized by the free stream sound velocity c_∞, where u, v, and w are velocity components in the streamwise x, wall-normal y, and spanwise z directions, respectively. The free stream Mach number $\mathrm{Ma} = U_0/c_\infty = 0.2$ with the free stream velocity U_∞ is sufficiently low for negligible compressibility effects. The inlet station from the leading edge of the plate x_0 is used as a reference length scale, and the inlet Reynolds number based on x_0 and U_∞ is $\mathrm{Re}_x = 10^5$. The time t is nondimensionalized by x_0/c_∞.

The DNS is computed in a rectangular domain with sizes $L_x \times L_y \times L_z = 9.6 \times 0.92 \times 0.6$ on a grid $N_x \times N_y \times N_z = 4096 \times 550 \times 512$. Here L_x, L_y, and L_z are sizes in three directions, and they are nondimensionalized by x_0; N_x, N_y, and N_z are the numbers of grid points in three directions. In order to trigger the transition, Tollmien-Schlichting (TS) waves and oblique waves are introduced within a narrow disturbance strip near the inlet. The streamwise width $l_0 = 0.2$ of the disturbance strip equals to the streamwise wavelength λ_x of the initial TS waves, and the spanwise wavelength of the oblique wave is $\lambda_z = 0.15$.

A schematic diagram for the implementation of VSFs in boundary-layer transition is presented in Fig. 2. In order to capture the generation of turbulent spots and reduce the computation cost, the vorticity field in the computational subdomain Ω is extracted at separate times and different streamwise locations from the entire DNS datesets. The VSFs are then calculated in the extracted subdomains in a series of sliding windows. In the implementation, six windows are applied to six instantaneous DNS fields, and the window parameters are listed in Table I. Here l_x denotes the streamwise width of a sliding window, x_c denotes the center of the streamwise locations of the window, and $\Delta t \equiv t - t_0$ denotes a tracking time interval, where t_0 is the time for the first window W1 in Table I.

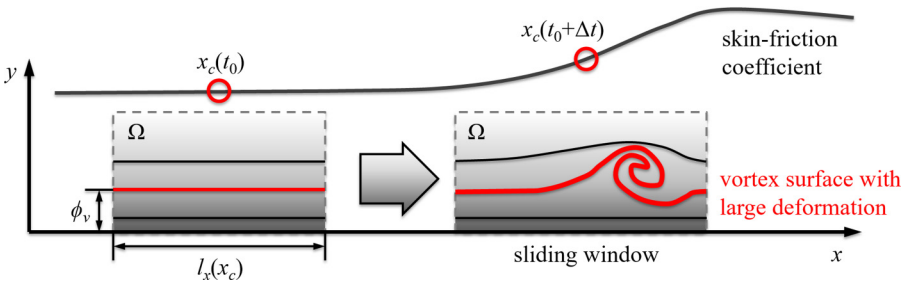

FIG. 2. A sketch of the evolution of vortex surfaces (solid lines) in sliding windows in boundary-layer transition along with the rise of the skin-friction coefficient.

As sketched in Fig. 2, the sliding window with increasing x_c moves and stretches in the streamwise direction during transition. The window parameters in Table I are chosen to ensure that the major deformation of vortex surfaces, whose streamwise extent in the laminar stage is l_0, can be captured within the compact sliding window with large enough $l_x > \lambda_x = l_0$ [34]. The window height $l_y = 0.058$ is about two boundary-layer thicknesses at the transition point around $x = 2.4$, so that the nearly laminar field without vortical structures in the outer layer is excluded. The window width is $l_z = \lambda_z$ with $-l_z/2 \leqslant z \leqslant l_z/2$, and the initial flow is symmetric with $z = 0$. Thus the sliding window encloses the evolution of the vortical structures generated from one initial TS wavelength, and the computation domain for VSF calculation is reduced to make the computational cost feasible.

Since Eq. (2) is a pure advection equation driven by $\boldsymbol{\omega}$, the high resolution of ϕ_v and smooth $\boldsymbol{\omega}$ are required to achieve a smooth VSF solution. Otherwise the computed VSF isosurfaces can be underresolved or corrugated. The grid resolution for calculating VSFs in a sliding window is refined as $N_x \times N_y \times N_z = 768 \times 768 \times 768$. The vorticity field is interpolated from the original DNS data and is filtered in physical space using Simpson's rule [35] for smoothing slight spatial oscillations owing to the fourth-order finite difference scheme in DNS. The filter width is $\Delta_f = 4[\Delta_x \Delta_y(y) \Delta_z]^{1/3}$, where Δ_x, Δ_y, and Δ_z denote the DNS grid spacing in streamwise, wall-normal, and spanwise directions, respectively. A sensitivity study was performed to determine the VSF grid resolution and the filter width. We find that the VSF deviation decreases with increasing VSF resolution, and the present grid makes a compromise between the acceptable accuracy and computational cost of the VSF solution. Moreover, the filter width is selected to smooth the spatial oscillation without eliminating fine-scale vortical structures.

C. Construction of VSFs in boundary-layer transition

The VSF is calculated from the instantaneous vorticity field in each sliding window. We remark that the nearly laminar velocity-vorticity field with wall-parallel vortex lines and ϕ_{v0} at the lateral boundary of a sliding window are almost unaltered during the time period in the present study. Thus the VSF obtained from the boundary-constraint method at separate DNS snapshots is consistent with the numerical solution calculated from the two-time method, which is nearly equivalent to describe the temporal evolution of VSFs using a series of temporally resolved velocity fields [32]. At the mean time, the computational cost of the boundary-constrained method can be several orders of magnitude less than that of the two-time method.

TABLE I. The window width, streamwise location, and tracking time interval of sliding windows.

Window	W1	W2	W3	W4	W5	W6
l_x	0.21	0.25	0.29	0.40	0.42	0.54
x_c	2.50	2.67	2.73	2.88	3.14	3.33
Δt	0	0.028	0.037	0.055	0.082	0.10

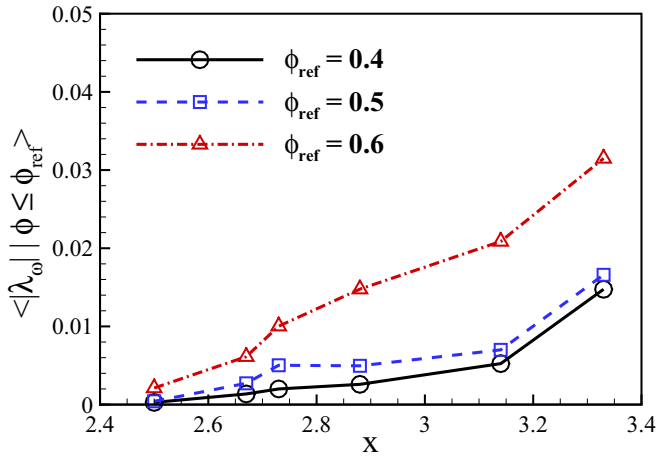

FIG. 3. The conditional averaged deviation $\langle|\lambda_\omega| \,|\, \phi \leqslant \phi_{\text{ref}}\rangle$ of near-wall VSFs with different ϕ_{ref} in six sliding windows along $x = x_c$.

In the computation of ϕ_v, the boundary condition Eq. (3) is applied in the spanwise direction. Dirichlet boundary conditions $\phi_v = 0$ at the wall $y = 0$ and $\phi_v = 1$ at $y = l_y$ are applied in the wall-normal direction. Extra ghost zones are added in the streamwise direction where vortex lines are artificially stretched to be parallel to streamwise boundaries, so that periodic boundary conditions of ϕ_v can be applied. The initial VSF at $\tau = 0$ in Eq. (4) is set as $\phi_{v0} = y/l_y$, which ensures that the VSF is invariant in mean shear flows and is compatible with boundary conditions [24]. The isocontour level of $0 \leqslant \phi_v \leqslant 1$ represents the scaled wall distance of the wall-parallel vortex surfaces in the stage before transition.

The deviation of a VSF solution from an exact VSF is quantified by $\lambda_\omega \equiv (\boldsymbol{\omega} \cdot \nabla\phi_v)/(|\boldsymbol{\omega}||\nabla\phi_v|)$ [28], which represents the cosine of the angle between the vorticity and the scalar gradient. An exact VSF solution has $\lambda_\omega = 0$ everywhere, and an approximate VSF solution with a reasonable accuracy level should have low VSF deviation as $\langle|\lambda_\omega|\rangle < 5\%$ or 10%, where $\langle\cdot\rangle$ denotes the volume average over the domain of VSF calculation. The averaged VSF deviation $\langle|\lambda_\omega| \,|\, \phi \leqslant \phi_{\text{ref}}\rangle$ conditioned on different near-wall level sets $\phi_v \leqslant \phi_{\text{ref}}$ in each sliding window is shown in Fig. 3. The averaged VSF deviation is very small (less than 4%), indicating that the vortex surfaces in near-wall regions are accurately represented by VSF isosurfaces. The deviation increases with x, because the geometry and topology of vortex lines become more convoluted during transition and the convergence of VSF deviation becomes slower [32]. In addition, $\langle|\lambda_\omega| \,|\, \phi \leqslant \phi_{\text{ref}}\rangle$ increases with ϕ_{ref}, because $|\boldsymbol{\omega}|$ in outer layers is close to zero and the weak oscillating vorticity causes the relatively large deviation in outer layers. The VSF isosurfaces remote from the wall, however, are not important in transition dynamics and are not displayed in following VSF visualization.

To achieve the small averaged VSF deviation, the corresponding T_τ in the implementation is 0.26 with $O(10^5)$ pseudotime steps. The typical computational cost for calculating the VSF in a window is $O(10^2)$–$O(10^3)$ CPU hours, depending on the complexity of vorticity, on 192 Intel Xeon E5 processor cores on the TH-2A supercomputer in Guangzhou, China. It is still computationally expansive and needs to improve in future work.

III. EVOLUTION OF VSFs IN THE GENERATION OF TURBULENT SPOTS

A. Generation of hairpin-like bulges

We use VSF isosurfaces to study the evolution of vortex surfaces in the generation of turbulent spots. The isosurfaces with the same initial planar geometry and different initial wall-distances can have different evolutionary geometries in their evolution. As sketched in Fig. 2, the isosurfaces very

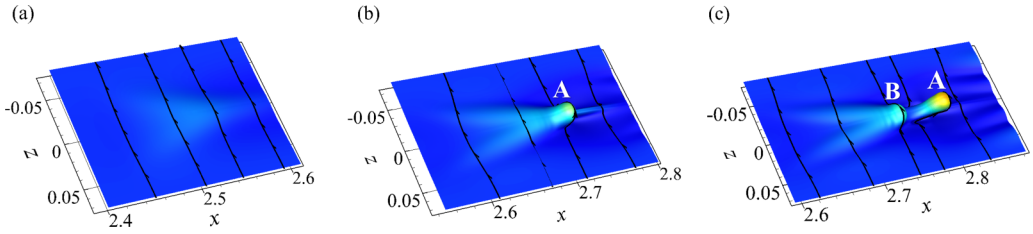

FIG. 4. Evolution of the isosurface of $\phi_v = 0.2$ before the inception of turbulent spots in sliding windows (a) W1, $x_c = 2.50$, (b) W2, $x_c = 2.67$, and (c) W3, $x_c = 2.73$. The isosurfaces are color coded by the wall-normal distance from blue to red, and vortex lines are integrated from the surfaces.

close to the wall with $\phi_v < 0.05$ or remote from the wall with $\phi_v > 0.5$ have only slight deformation owing to the relatively small disturbances in both regions. On the other hand, the isosurfaces from the near-wall region can evolve into complex shapes with the maximum deformation [24], and they are used to characterize the structural evolution in transition.

In Fig. 4 VSF isosurfaces of a fixed contour value $\phi_v = 0.2$ at three different windows and times display the generation of the signature hairpin-like structure before the inception of turbulent spots. As the averaged VSF deviation is very small in Fig. 3, vortex lines are almost attached on the VSF isosurfaces. From an initial planar vortex surface parallel to the wall, the vortex surface first forms a triangular bulge in Fig. 4(a) and then evolves into the primary hairpin-like structure with rolling up of lateral edges of the bulge in Fig. 4(b). Subsequently the primary hairpin-like structure labeled by "A" is stretched and elevated, and the hairpin "head" A is detached from the original bulge under the effects of the mean shear and the self-induced motion of vortical structures in Fig. 4(c).

The generation process of the primary and secondary hairpin-like bulges in Fig. 4 is very similar to that in transitional channel flow (as sketched in Fig. 22 in Ref. [24]), which has been elucidated from reduced model vorticity equations with the Helmholtz vorticity theorem and the Biot-Savart law, but subsequent evolutions of VSFs in transitional channel flows and boundary layers are essentially different. The channel flow has the intrinsic symmetry in the wall-normal direction, so if the channel is long enough, vortex reconnection will eventually occur between hairpin-like bulges elevated from opposite walls in transition [30] at low and moderate Reynolds numbers, and then the hairpin-like structures are destroyed. On the other hand, this type of vortex reconnection cannot occur in boundary-layer transition, and clear turbulent spots will be generated owing to interactions of coherent structures in streamwise and spanwise directions, which will be elaborated in following subsections.

In Fig. 5 we also display the evolution of isosurfaces of the Q criterion [20]. In contrast to using the fixed isocontour value in Fig. 4, we have to intentionally adjust the threshold of $Q/Q_{\max}$ to display the structures at intermediate scales with some time coherence, where $Q_{\max}$ is the maximum value

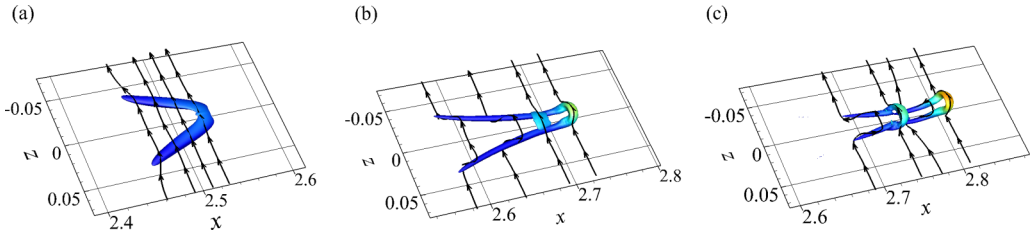

FIG. 5. Evolution of the isosurface of the Q criterion with different isocontour values before the inception of turbulent spots in sliding windows (a) W1, $x_c = 2.50$, $Q = 0.5Q_{\max}$, (b) W2, $x_c = 2.67$, $Q = 0.05Q_{\max}$, and (c) W3, $x_c = 2.73$, $Q = 0.05Q_{\max}$. The isosurfaces are color-coded by the wall-normal distance from blue to red, and vortex lines are integrated from the surfaces.

of Q in each sliding window. Since vortex lines are significantly misaligned with the Q isosurfaces, the structural evolution of Q cannot be directly explained by the vorticity equation and related vortex dynamics. By utilizing the VSF, Zhao *et al.* [24] found that the tubelike "vortex cores" identified by Q or other Eulerian vortex criteria are formed by rolling up of initially planar vortex surfaces as displayed in Fig. 4 with significant vorticity intensification. This formation process of the tubelike axial vortices can be considered as a nontrivial three-dimensional extension of rolling up of vortex sheets which was analyzed in two-dimensional theoretical models [36].

B. Sinuous distortion of vortex surfaces

The evolution of VSF isosurfaces in the inception and growth of turbulent spots is shown in Fig. 6. The volumetric rendering is used to display the deformation of the isosurfaces at a range of ϕ_v from 0.05 to 0.4. The bulges of vortex surfaces, as "hairpin heads," are labeled by capital letters, and lower wavy vortex surfaces, as "streaks," are labeled by dashed lines. In particular, the secondary hairpin head and the nearby distorted streak, which are two typical objects in the present structure tracking, are labeled by yellow and light blue circles, respectively.

The primary and secondary hairpin-like structures labeled by "A" and "B" are stretched from the triangular bulges with elongated "legs" in the streamwise direction, and the tertiary hairpin "C" in Fig. 6(a) and more hairpins "D," "E,', "F," and "G" in Fig. 6(b) are induced to form a elongated packet or train of hairpins as an autoregeneration process [3].

The VSF isosurfaces shown in Figs. 6(a) and 6(c) in adjacent sliding windows (also see Table I) for two consecutive TS-wave periods can be combined as a whole structure at the same time. The streaky structure in the upstream of the primary hairpin A around $x = 3$ and $z = \pm 0.05$ in Fig. 6(a) is a wake structure in the downstream of the "legs" around $x = 3.1$ of hairpin bulges F and G in Fig. 6(c). In Fig. 6(a), the structure packet along with the spanwise symmetric plane $z = 0$ moves faster than nearby wake streaks from the prior TS period, because hairpin heads have larger y and streamwise velocity u than near-wall streaks. This velocity difference causes the end-to-end connection between two structure packets originally at two consecutive TS-wave periods. The overlap region of the connection grows from $x > 2.9$ in Fig. 6(a) to $x > 3.1$ in Fig. 6(c) during transition, which is also related to the further hairpin-streak interaction discussed below.

In Fig. 6(b), the hairpin train approaches and then passes by nearby streaks. Here wavy near-wall vortex surfaces with the oscillating wall-normal vorticity identify high- and low-speed streaks labeled in Fig. 6 [11,14]. As shown in Fig. 7(a), the wavy vortex surfaces around $2.7 < x < 2.8$ and $2.95 < x < 3.05$ have oscillating ω_y dominated by $\partial u/\partial z$ as spanwise shear layers between the streaks on the near-wall x-z slice at $y = 0.01$.

The train of hairpin-like bulges consisting of Ω-shaped vortex lines (see Figs. 4 and 8) induces the spanwise velocity with alternating signs by the Biot-Sarvart law, as shown near $z = 0$ in Fig. 7(a). The perturbation of oscillating w on the flank of streaks triggers the Kelvin-Helmholtz (K-H) instability in the z direction, and the spanwise K-H instability causes the straight streaks very close to the hairpin train around $2.95 < x < 3.05$ and $z = \pm 0.025$ in Figs. 6(a) and 7(a) to rapidly distort into sinuous streaks around $3.1 < x < 3.25$ and $z = \pm 0.025$ in Figs. 6(b) and 7(b). In Fig. 7(b) the spanwise shear layers coincide with the oscillating spanwise velocity shown by the alternating solid and dashed contour lines. Additionally, a close-up view for the sinuous distortion is displayed in Figs. 8(a) and 8(b).

The lateral growth of young turbulent spots was observed in the visualization of experiments [37] and large-scale DNS [19], and the mechanism of the lateral growth was explained as the destabilization of the surrounding streaks. As a more detailed explanation, we find that the sinuous distortion of the near-wall wavy vortex surfaces can be one of the critical mechanisms in the lateral growth. On the other hand, the sinuous distortion cannot be identified from the evolution of isosurfaces of Q in Fig. 9 owing to the lack of time coherence and incomplete visualization of vortex surfaces. We only observe that some small-scale structures are generated near the hairpin train in Fig. 9. This observation sometimes was simply interpreted as the visual "breakdown" of large-scale vortices.

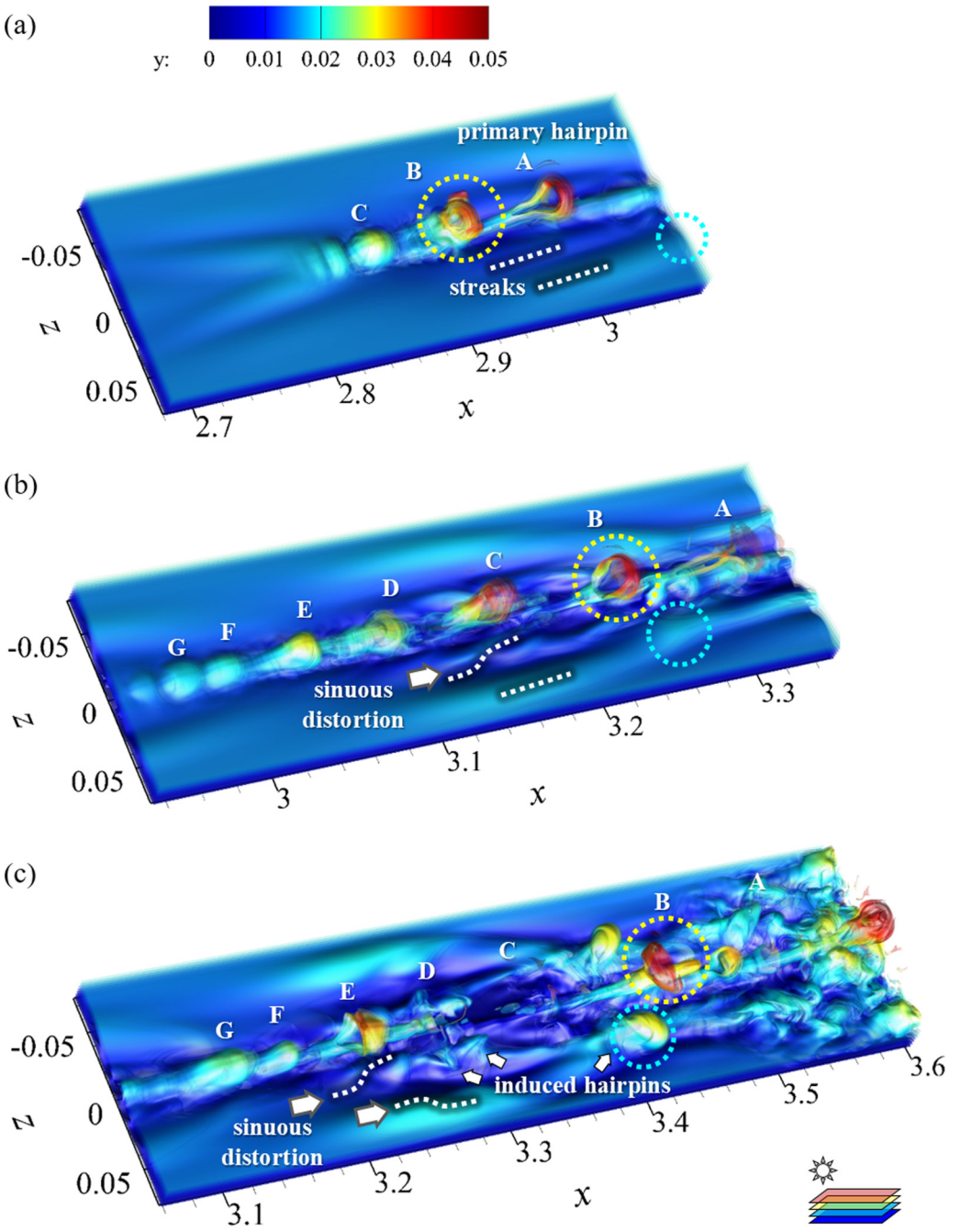

FIG. 6. Evolution of isosurfaces of $0.05 \leqslant \phi_v \leqslant 0.4$ in the generation of turbulent spots in sliding windows (a) W4, $x_c = 2.88$, (b) W5, $x_c = 3.14$, and (c) W6, $x_c = 3.33$. The VSF isosurfaces are color-coded by wall-normal distance. The translucency of the surfaces is increased from 20% for $\phi_v = 0.05$ to 90% for $\phi_v = 0.4$. This volumetric rendering is sketched in the bottom right schematic diagram. The hairpin heads are labeled by capital letters, and streaks are labeled by dashed lines. The secondary hairpin head and the nearby distorted streak, which are two typical objects in the structure tracking, are labeled by yellow and blue circles, respectively.

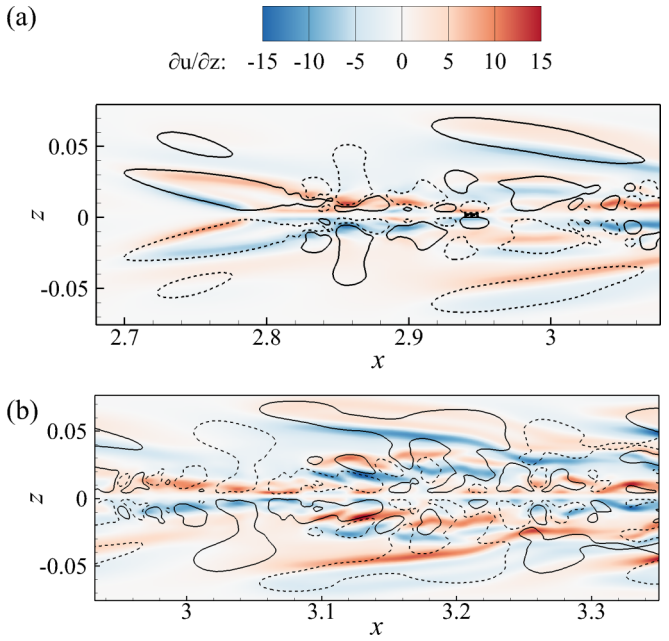

FIG. 7. Contours of the spanwise shear $\partial u/\partial z$ and contour lines of the spanwise velocity $w = 0.005$ (solid lines) and $w = -0.005$ (dashed lines) on near-wall x-z slices at $y = 0.01$ in sliding windows (a) W4, $x_c = 2.88$ and (b) W5, $x_c = 3.14$.

Nonetheless, the underlying physical mechanism of this abrupt process appears to be elusive in terms of vortex dynamics.

C. Spreading of sinuous distortion

Subsequently, the distorted vortex surface with the growing magnitude of sinuous motion forms a train of skewed, incomplete hairpin-like structures around $3.2 < x < 3.4$ and $z = \pm 0.025$ in Fig. 6(c). The similar generation process of near-wall quasistreamwise vortices from straight streaks

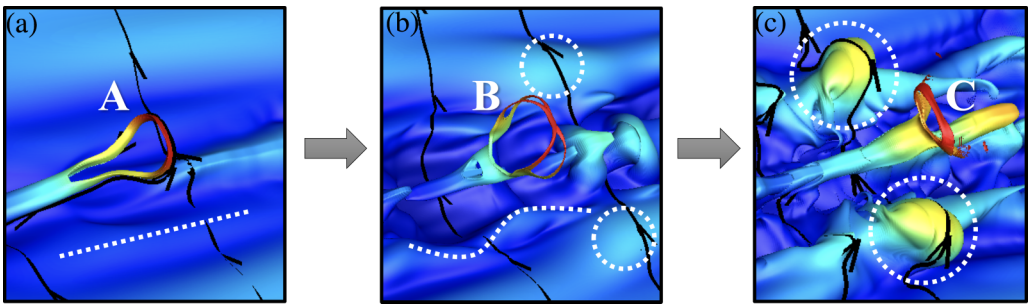

FIG. 8. A close-up view for the generation process of sinuous distortion and a pair of new hairpin-like bulges. Some portions of the VSF isosurface $\phi_v = 0.28$ are extracted from Fig. 6. (a) W4, $x_c = 2.88$, (b) W5, $x_c = 3.14$, and (c) W6, $x_c = 3.33$. The surfaces are color-coded by wall-normal distance. The hairpin heads are labeled by capital letters, and streaks are labeled by dashed lines. The new hairpin-like bulges generated when the primary hairpin train passes by adjacent streaks are labeled by circles. Some vortex lines are integrated from the surfaces.

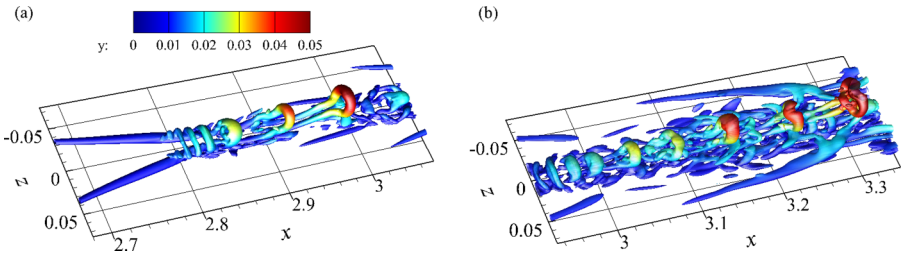

FIG. 9. Isosurfaces of $Q = 0.01 Q_{\max}$ in sliding windows (a) W4, $x_c = 2.88$ and (b) W5, $x_c = 3.14$. The surfaces are color-coded by the wall-normal distance from blue to red.

perturbed by spanwise velocity was observed in the DNS of minimal channel flow [15] and was explained by the streak-transient-growth mechanism [14] with an analysis based on vortex lines. This secondary train of hairpins regenerates the spanwise perturbation around $z = \pm 0.025$ in Fig. 7(b) as the primary one along $z = 0$, and the perturbation also triggers the spanwise K-H instability on neighboring streaks around $z = \pm 0.05$ to further distort spanwise wavy vortex surfaces into more sinuous streaks with quasistreamwise vortices. In addition, we observe that hairpin head B labeled in yellow circles gradually passes by the adjacent streak labeled in blue circles in a series of windows in Fig. 6. The interaction between the "hairpin head" and adjacent "streaks" produces a pair of new hairpin-like bulges on both sides of hairpin B and around $x = 3.4$ in Fig. 6(c). A close-up view for the generation of the new hairpin-like bulges is displayed in Figs. 8(b) and 8(c).

In Fig. 10 the spreading of the sinuous distortion of vortex surfaces is also illustrated as the growing oscillation of VSF contour lines of $\phi_v = 0.2$ on y-z slices at the upstream side of hairpin-like bulges with increasing x. The rolling up of vortex surfaces in the generation of hairpin-like bulges on the y-z planes is accompanied with the creation of the streamwise vorticity ω_x. Moreover, reconnection of vortex surfaces around $z = 0$ and the "neck" of hairpin-like bulges is observed from the topological change of VSF contour lines of $\phi_v = 0.4$ in Fig. 10(d).

In sum, the mechanism of the spanwise propagation of sinuous distortion appears to lead to the mass production of hairpin-like structures and significantly accelerates the lateral growth of young turbulent spots. This process could be a cycling mechanism of scale cascade in the growth of turbulent spots and finally spreads the distortion on the entire vortex surface to form turbulent-like structures, e.g., the small-scale structures in the downstream around $3.5 < x < 3.6$ in Fig. 6(c). Furthermore, Goldstein *et al.* [26] observed that the spreading of turbulent spots is only confined to the periphery

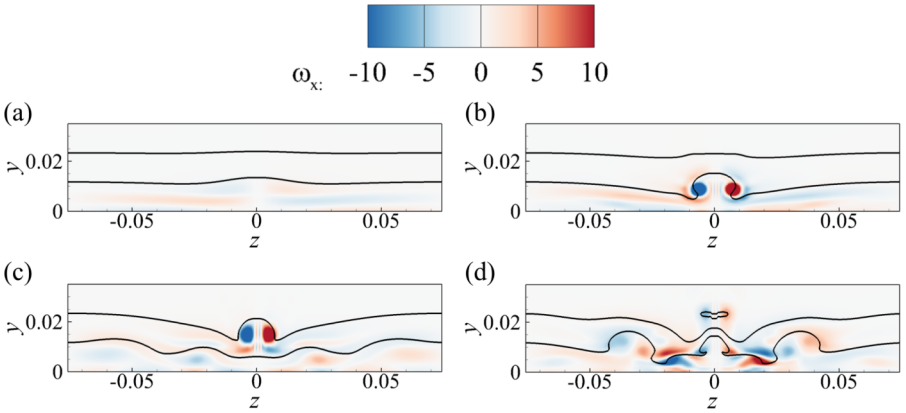

FIG. 10. Contours of the streamwise vorticity ω_x and contour lines of $\phi_v = 0.2$ and $\phi_v = 0.4$ on $y - z$ slices at (a) $x = 2.55$ in W1, (b) $x = 2.77$ in W3, (c) $x = 2.95$ in W4, and (d) $x = 3.27$ in W5.

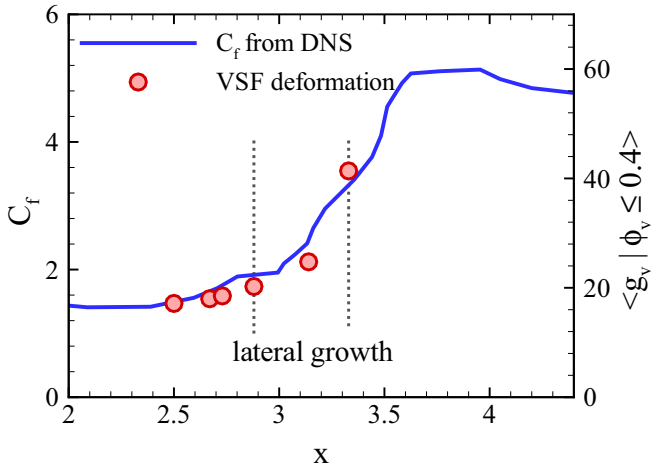

FIG. 11. The rise of the wall-friction coefficient and the deformation of near-wall VSF isosurfaces in the growth of turbulent spots, where the temporally averaged C_f was reported in the DNS study [31] and near-wall VSF deformation $\langle g_v|\phi_v \leqslant 0.4\rangle$ is calculated in six sliding windows at different $x = x_c$. The region of the lateral growth of turbulent spots is labeled between dotted lines.

of the spot, so they also concluded that the lateral spreading of turbulent spots is a self-similar process. Therefore, although the present study focuses on the generation of a young turbulent spot, the spreading mechanism of sinuous distortion may be applied to more developed spots. We remark that it is worth examining the role of the sinuous distortion in different transitional boundary layers; e.g., one could test whether the spreading of turbulent spots can be controlled by locally suppressing the sinuous distortion near the hairpin train in DNS.

D. Quantification of VSF deformation

The deformation of near-wall VSF isosurfaces shown in Figs. 4 and 6 is quantified by $\langle g_v|\phi_v \leqslant 0.4\rangle$ with $g_v \equiv |\nabla\phi_v|$ in six windows at different $x = x_c$ in Fig. 11. We find a coincidence of the rising wall-friction coefficient C_f and $\langle g_v|\phi_v \leqslant 0.4\rangle$ during the transition, where the temporally averaged C_f was reported in the DNS study [31]. This observation implies that the drag production is highly correlated with the VSF deformation.

Furthermore, the spatial distribution of the near-wall VSF deformation is shown in Fig. 12. The streamwise evolution of the deformation of near-wall VSF isosurfaces is quantified by $\langle g_v|x,\phi_v \leqslant 0.4\rangle$ at four different windows in Fig. 12(a). The deformation of vortex surfaces increases along x, which agrees with the observations in Figs. 4 and 6. In particular, the double peaks of the dashed-dotted line in the zoom-in window in Fig. 12(a) quantify the primary and secondary hairpin-like bulges in Fig. 4(c), and the triple peaks of the dashed line quantify hairpin-like bulges A, B, and C in Fig. 6(a). The migration of the peaks and the increasing spacing between the peaks indicate that the hairpin-like structures and the entire structure packet are stretched in the streamwise direction.

The spanwise distortion of near-wall VSF isosurfaces in the lateral growth of turbulent spots is quantified by $\langle g_v|z,\phi_v \leqslant 0.4\rangle$ at different z and $x = x_c$ in Fig. 12(b). Since the VSF deformation is almost symmetric with $z = 0$, it is only displayed at $z \geqslant 0$. The large VSF deformation is confined in $-0.02 \leqslant z \leqslant 0.02$ at $x_c < 2.88$, corresponding to the formation of the hairpin train in Figs. 4, 6(a), and 10(a)–10(c), and then it rapidly spreads out with the sinuous distortion of vortex surfaces in Figs. 6(b) and 6(c) and 10(d). The lateral growth of turbulent spots also coincides with the surge of C_f at $2.73 \leqslant x \leqslant 3.33$ labeled in Fig. 11 and the surge of $\langle g_v|x,\phi_v \leqslant 0.4\rangle$ in Fig. 12(a).

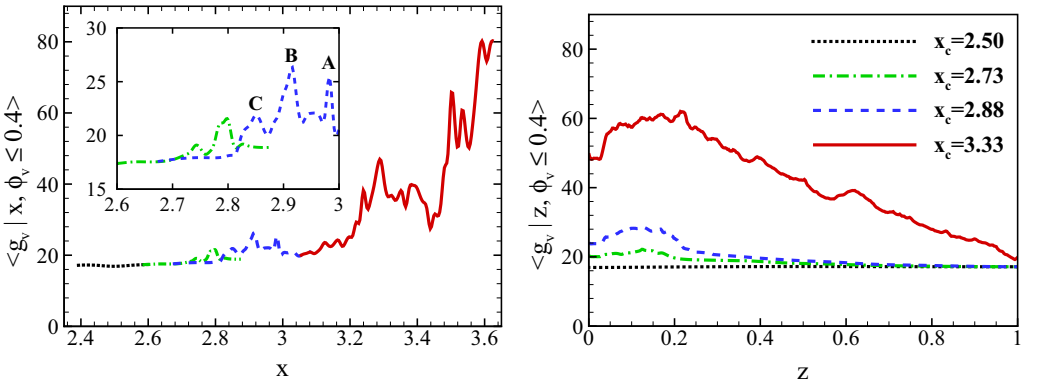

FIG. 12. The deformation of near-wall VSF isosurfaces calculated in four windows (W1, W3, W4, and W6) in the growth of turbulent spots. (a) Distribution of $\langle g_v | x, \phi_v \leqslant 0.4 \rangle$ in the streamwise direction at different $x = x_c$; (b) distribution of $\langle g_v | z, \phi_v \leqslant 0.4 \rangle$ in the spanwise direction at different $x = x_c$.

E. Remarks on structure-identification methods

The interpretation on the generation mechanism of turbulent spots depends on the coherent structures visualized by different identification methods. The structures identified by the isosurfaces of conventional u and the Q criterion [20] at $x_c = 3.33$ are shown in Fig. 13 for comparison. The isosurface of u displays only sinuous streaks very close to the wall, which is similar to the bottom portion of VSF isosurfaces in Fig. 6(c). The isosurface of Q displays only hairpin-like vortex cores, which is similar to the upper portion of VSF isosurfaces in Fig. 6(c). Thus it is interesting that the superposition of the isosurfaces of u and Q, as a composite structure in Fig. 13(c), appears to resemble the VSF isosurfaces in Fig. 6(c). We remark that hairpin heads A, C, and D are blurring in Fig. 6(c) owing to the dissipative numerical regularization, but it can be improved by increasing the VSF grid resolution. Additionally, the similar hairpin-streak interaction is also observed in the bypass boundary-layer transition if we superpose the isosurfaces of the temperature and the swirling strength [3] in Fig. 1 and supplemental movies S1 and S2 in Ref. [19].

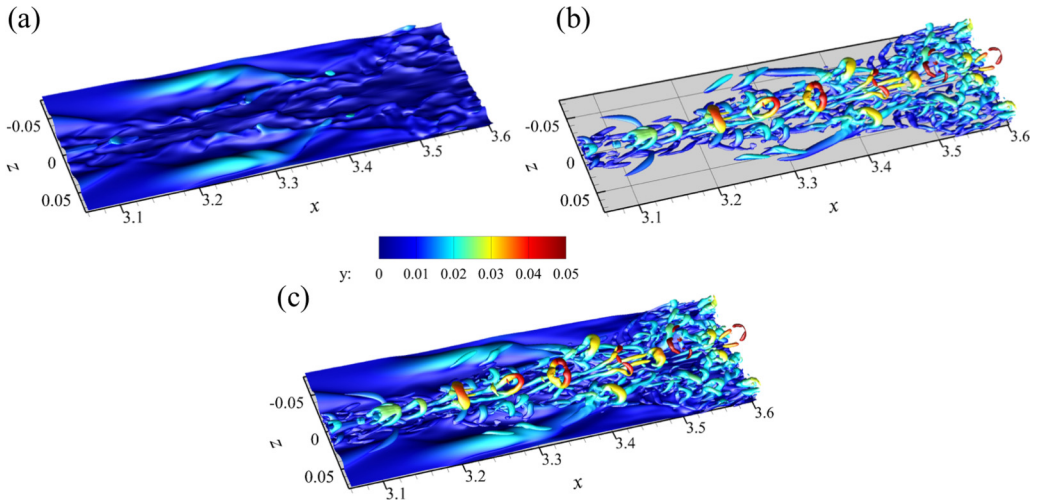

FIG. 13. Isosurfaces of u and Q in the sliding window W6 at $x_c = 3.33$. (a) Isosurface of $u = 0.1$, (b) isosurface of $Q = 0.01\,Q_{\max}$, (c) superposition of the isosurfaces of u and Q in Figs. 13(a) and 13(b).

TABLE II. Typical flow structures identified by different methods in K-type transitional wall flows in the literature, and corresponding geometries of vortex surfaces with their generation mechanisms investigated in the present study and former ones [24,30].

Typical flow structure	Geometry of the vortex surface with generation mechanism
Laminar shear flow	Wall-parallel planar surface
Λ-like structure	Triangular bulge from wall-normal disturbed surface in shear flow
Hairpin and packet	Hairpin bulges from rolling up and stretching of triangular bulge
Streak	Wavy surface at downstream of hairpin "legs"
Turbulent spot	Sinuous distortion of wavy surface from hairpin-streak interaction
Breakdown to turbulence	Fully distorted surface owing to all the mechanisms above

On the other hand, neither the isosurface of u nor Q can reveal complete vortex surfaces and elucidate the whole dynamical process in the structural evolution. Furthermore, the isocontour levels of u and Q have to be carefully selected to seek the structures with presumed geometry and time coherence. The subjectivity introduced in the threshold selection and structure-identification methods can result in the debate and confusion in the structure characterization in the literature. By contrast, we use the same level sets of the evolving VSF to display the Lagrangian-like evolution of the integrated vortex-surface structure from the laminar stage to the late transitional stage, rather than using different identification methods with varied isocontour levels in the studies from the Eulerian view.

Thus we can elucidate most of the important structures and their generation mechanisms using the vortex surface, as a single structure object, in the Lagrangian framework of structural evolution. Typical Eulerian structures and their corresponding geometries of vortex surfaces with inception mechanisms are summarized in Table II.

IV. CONCLUSIONS

The VSF is extended to elucidate the generation mechanism of turbulent spots in the K-type transitional boundary layer from a Lagrangian view. The boundary-constraint method is developed to construct VSFs in a series of sliding windows. The windows extract instantaneous vorticity fields at different times and streamwise locations, and they contain evolving flow structures whose streamwise extent in the laminar stage is equal to the streamwise wavelength of the initial TS waves.

The visualization of VSF isosurfaces displays the Lagrangian-like evolution of vortex surfaces consisting of vortex lines with different wall distances in the laminar state. We label and track the signature coherent structures in a time series of evolving vortex surfaces. Then we observe the order of important events in the generation of young turbulent spots and explain the underlying flow physics of each event.

First the near-wall VSF isosurfaces evolve from wall-parallel planar vortex surfaces into a train of hairpin-like structures. In the inception of turbulent spots, the train of bulges of vortex surfaces (or "hairpin heads") consisting of Ω-shaped vortex lines induce sinuous distortion, via the Biot-Sarvart law, on lower wavy vortex surfaces (or "streaks"), and then triggers the K-H instability in the spanwise direction. The sinuous distortion increases in the streamwise direction and propagates in the lateral direction, which can lead to the mass production of small-scale, skewed hairpin-like structures and the rapid lateral growth of turbulent spots. This process appears to be a cycling mechanism of scale cascade towards the fully turbulent state in boundary-layer transition. We remark that the "streak" and "hairpin" structures frequently mentioned in the literature have strong interactions in the present K-type transition, but they can be interpreted as different evolutionary geometries of the same set of vortex surfaces at different spatial regions and times, rather than considering them as two different elementary structures visualized by different structure identification methods.

Furthermore, the surge of the skin-friction coefficient is highly correlated to the near-wall VSF deformation in the lateral growth of turbulent spots. This quantitative result supports that the sinuous distortion of vortex surfaces plays an important role during transition and implies that it is possible to develop a model of C_f based on the structural evolution. Additionally, the increase of C_f can be correlated with the statistical feature of other structure-identification methods, which can be considered in further work.

Although the present study is restricted to the K-type natural transition, the VSF with the boundary-constraint method can be applied to other cases, e.g., the Herbert-type [31] and the bypass [19] boundary-layer transitions as well as pipe transition [38] to explore whether universal flow structures or processes exist in the transitions in canonical wall-bounded flows.

ACKNOWLEDGMENTS

The authors thank P. Hack and J. Kim for their assistance on accessing the DNS data at CTR and X. Wu for helpful discussions. Numerical simulations were carried out on the TH-2A supercomputer in Guangzhou, China. This work has been supported by the NSFC (Grants No. 11522215, No. 91541204, and No. 11472015), the 2016 CTR Summer Research Program at Stanford University, and the Thousand Young Talent Program of China.

[1] R. J. Adrian, Hairpin vortex organization in wall turbulence, Phys. Fluids **19**, 041301 (2007).
[2] J. Zhou, R. J. Adrian, and S. Balachandar, Autogeneration of near-wall vortical structures in channel flow, Phys. Fluids **8**, 288 (1996).
[3] J. Zhou, R. J. Adrian, S. Balachandar, and T. M. Kendall, Mechanisms for generating coherent packets of hairpin vortices in channel flow, J. Fluid Mech. **387**, 353 (1999).
[4] B. A. Singer and R. D. Joslin, Metamorphosis of a hairpin vortex into a young turbulent spot, Phys. Fluids **6**, 3724 (1994).
[5] A. H. Haidari and C. R. Smith, The generation and regeneration of single hairpin vortices, J. Fluid Mech. **277**, 135 (1994).
[6] B. A. Singer, Characteristics of a young turbulent spot, Phys. Fluids **8**, 509 (1996).
[7] S. J. Kline, W. C. Reynolds, F. A. Schraub, and P. W. Runstadler, The structure of turbulent boundary layers, J. Fluid Mech. **30**, 741 (1967).
[8] F. Waleffe, On a self-sustaining process in shear flows, Phys. Fluids **9**, 883 (1997).
[9] S. C. Reddy, P. J. Schmid, J. S. Baggett, and D. S. Henningson, On stability of streamwise streaks and transition thresholds in plane channel flows, J. Fluid Mech. **365**, 269 (1998).
[10] P. Andersson, L. Brandt, A. Bottaro, and D. S. Henningson, On the breakdown of boundary layer streaks, J. Fluid Mech. **428**, 29 (2001).
[11] P. Schlatter, L. Brandt, H. C. de Lange, and D. S. Henningson, On streak breakdown in bypass transition, Phys. Fluids **20**, 101505 (2008).
[12] T. A. Zaki and P. A. Durbin, Mode interaction and the bypass route to transition, J. Fluid Mech. **531**, 85 (2005).
[13] P. Durbin and X. Wu, Transition beneath vortical disturbances, Annu. Rev. Fluid Mech. **39**, 107 (2007).
[14] W. Schoppa and F. Hussain, Coherent structure generation in near-wall turbulence, J. Fluid Mech. **453**, 57 (2002).
[15] Y. Wang, W. Huang, and C. Xu, On hairpin vortex generation from near-wall streamwise vortices, Acta Mech. Sinica **31**, 139 (2015).
[16] A. Schröder and J. Kompenhans, Investigation of a turbulent spot using multi-plane stereo particle image velocimetry, Exp. Fluids **36**, 82 (2004).

[17] A. Schröder, R. Geisler, G. E. Elsinga, F. Scarano, and U. Dierksheide, Investigation of a turbulent spot and a tripped turbulent boundary layer flow using time-resolved tomographic PIV, Exp. Fluids **44**, 305 (2008).
[18] J. R. Brinkerhoff and M. Yaras, Numerical investigation of the generation and growth of coherent flow structures in a triggered turbulent spot, J. Fluid Mech. **759**, 257 (2014).
[19] X. Wu, P. Moin, J. M. Wallace, J. Skarda, A. Lozano-Durán, and J. Hickey, Transitional-turbulent spots and turbulent-turbulent spots in boundary layers, Proc. Natl. Acad. Sci. USA **114**, E5292 (2017).
[20] J. C. R. Hunt, A. A. Wray, and P. Moin, Eddies, streams, and convergence zones in turbulent flows, Center for Turbulence Research Report CTR-S88, 193 (1988).
[21] J. Jeong and F. Hussain, On the identification of a vortex, J. Fluid Mech. **285**, 69 (1995).
[22] C. B. Lee and J. Z. Wu, Transition in wall-bounded flows, Appl. Mech. Rev. **61**, 030802 (2008).
[23] J. Kim and P. Moin, The structure of the vorticity field in turbulent channel flow. Part 2. Study of ensemble-averaged fields, J. Fluid Mech. **162**, 339 (1986).
[24] Y. Zhao, Y. Yang, and S. Chen, Evolution of material surfaces in the temporal transition in channel flow, J. Fluid Mech. **793**, 840 (2016).
[25] B. Rehill, J. Walsh, L. Brandt, P. Schlatter, T. A. Zaki, and D. M. McEligot, Identifying turbulent spots in transitional boundary layers, J. Turbomach. **135**, 011019 (2013).
[26] D. Goldstein, J. Chu, and G. Brown, Lateral spreading mechanism of a turbulent spot and a turbulent wedge, Flow Turbul. Combust. **98**, 21 (2017).
[27] B. Pierce, P. Moin, and T. Sayadi, Application of vortex identification schemes to direct numerical simulation data of a transitional boundary layer, Phys. Fluids **25**, 015102 (2013).
[28] Y. Yang and D. I. Pullin, On Lagrangian and vortex-surface fields for flows with Taylor-Green and Kida-Pelz initial conditions, J. Fluid Mech. **661**, 446 (2010).
[29] Y. Yang and D. I. Pullin, Evolution of vortex-surface fields in viscous Taylor-Green and Kida-Pelz flows, J. Fluid Mech. **685**, 146 (2011).
[30] Y. Zhao, Y. Yang, and S. Chen, Vortex reconnection in the late transition in channel flow, J. Fluid Mech. **802**, R4 (2016).
[31] T. Sayadi, C. W. Hamman, and P. Moin, Direct numerical simulation of complete H-type and K-type transitions with implications for the dynamics of turbulent boundary layers, J. Fluid Mech. **724**, 480 (2013).
[32] S. Xiong and Y. Yang, The boundary-constraint method for constructing vortex-surface fields, J. Comput. Phys. **339**, 31 (2017).
[33] G. S. Jiang and C. W. Shu, Efficient implementation of weighted ENO schemes, J. Comput. Phys. **126**, 202 (1996).
[34] W. Zheng, Y. Yang, and S. Chen, Evolutionary geometry of Lagrangian structures in a transitional boundary layer, Phys. Fluids **28**, 035110 (2016).
[35] K. C. Loh and J. A. Domaradzki, The subgrid-scale estimation model on nonuniform grids, Phys. Fluids **11**, 3786 (1999).
[36] J. Z. Wu, Vortex definition and "vortex criteria," Sci. China-Phys. Mech. Astron. **61**, 024731 (2018).
[37] M. Gad-el Hak, R. F. Blackwelder, and J. J. Riley, On the growth of turbulent regions in laminar boundary layers, J. Fluid Mech. **110**, 73 (1981).
[38] X. Wu, P. Moin, R. J. Adrian, and J. R. Baltzer, Osborne Reynolds pipe flow: Direct simulation from laminar through gradual transition to fully developed turbulence, Proc. Natl. Acad. Sci. USA **112**, 7920 (2015).